Surfaces and Interfaces 87 (2026) 109028

Contents lists available at ScienceDirect

Surfaces and Interfaces

journal homepage: www.sciencedirect.com/journal/surfaces-and-interfaces

Anisotropy by design in superconducting Nb thin films via ultrashort-pulse laser irradiation

Javier Frechilla [a], Nicolas Lejeune [b], Elena Martínez [a], Emile Fourneau [b], Alejandro Frechilla [a], Sergio Martín [a], Leonardo R. Cadorim [c,d], Luis A. Angurel [a], Germán F. de la Fuente [a], Alejandro V. Silhanek [b], Milorad V. Milošević [c,d], Antonio Badía-Majós [a,*]

[a] Instituto de Nanociencia y Materiales de Aragón (INMA), CSIC-Universidad de Zaragoza, Zaragoza, Spain
[b] Experimental Physics of Nanostructured Materials, Q-MAT, Université de Liège, Liège, Belgium
[c] COMMIT, Department of Physics, University of Antwerp, Groenenborgerlaan 171, B-2020, Antwerp, Belgium
[d] Stavropoulos Center for Complex Quantum Matter, Department of Physics and Astronomy, University of Notre Dame, Notre Dame, IN, USA

ARTICLE INFO

Keywords:
Laser induced periodic surface structure
Nb lattice parameter
Superconducting parameters
Magnetic flux penetration
Critical current density

ABSTRACT

The ability to fabricate anisotropic superconducting layers *à la carte* is desired in technologies such as fluxon screening or removal in field-resilient devices, flux lensing in ultra-sensitive sensors, or in templates for imprinting magnetic structures in hybrid magnetic/superconducting multilayers. In this work, laser processing is qualified as an enabling technology in the controllable fabrication of superconducting metasurfaces. Niobium thin films exposed to femtosecond ultraviolet laser pulses exhibit significant changes in their superconducting properties, directly connected with the observed surface topography, crystallite geometry, and lattice parameter modifications. On the mesoscopic scale, quasi-parallel periodic ripple structures (about 260 nm of spatial period) gradually form on the film surface by progressively increasing the laser energy per pulse, E_p. This gives way to a stepwise increase of the critical current anisotropy and magnetic flux channeling effects along the ripples. As demonstrated in our resistive and inductive measurements, these superstructures determine the electromagnetic response of the superconducting material. Time-dependent Ginzburg–Landau simulations corroborate the topographical origin of the customized anisotropy. Pulsed laser processing is promoted as a flexible, one-step, and scalable lithography-free technique for versatile surface functionalization in microelectronic superconducting technology.

1. Introduction

Niobium thin films are key components of a wide range of technologies, such as those involved in Josephson junctions, superconducting quantum interference devices (SQUID), microwave resonators, or radiofrequency superconducting cavities. The optimization and control of the crystallographic and superconducting properties of the films is thus essential and has been well reported in the literature [1–10]. Specifically, it has been found that the intrinsic superconducting properties of Nb (i.e., superconducting energy gap, magnetic penetration depth, and critical temperature, T_c) are dependent on dimensional parameters [1–3]. Thus, a noticeable reduction of T_c was observed when grain size [1] or film thickness [2] reduces below 30–50 nm. This behavior was attributed to finite-size effects (that is, length scales close to the coherence length of the material ξ), to changes in the electronic density of states or to the increase of film disorder. In general, induced stress and structural disorder, which vary with growth conditions of the film, may affect the critical temperature, the residual resistance ratio (RRR), and/or the lattice parameter of the Nb layer [1,2,4–7,10].

Along with the variation of the intrinsic superconducting properties, nano-patterning of Nb films, often required in device fabrication processes, may also produce changes in their magnetic flux pinning landscape, often relevant for applications. In particular, engineering of dedicated sample architectures at the nanometer scale opens the possibility of manipulating magnetic flux and has enabled the appearance of the so-called *fluxonic devices* [11–18], also emerging as a promising technology in cutting-edge applications as the quantum computation systems. Thus, the manipulation of magnetic flux by dedicated intervention in the mesoscopic scale, in particular through anisotropic surface patterns, allows fabrication of such devices as rectifiers [13],

* Corresponding author.
E-mail address: anabadia@unizar.es (A. Badía-Majós).

https://doi.org/10.1016/j.surfin.2026.109028
Received 23 December 2025; Received in revised form 23 February 2026; Accepted 16 March 2026
Available online 17 March 2026
2468-0230/© 2026 The Authors. Published by Elsevier B.V. This is an open access article under the CC BY-NC-ND license (http://creativecommons.org/licenses/by-nc-nd/4.0/).

filters [17], and fluxon lenses and diodes [19]. Another topical issue in superconducting devices is the unwanted presence of penetrating Abrikosov vortices, which may cause noise, distort the response of Josephson junctions, or even take place in the form of catastrophic flux avalanches in radiofrequency devices [20]. Among other strategies to drive flux out of the device, the proposal of using patterned superconducting layers with ratchet thickness profiles (typical length scales in the submicron range) came into the scene in the late 90's [12]. While it is still under development [21] from the theoretical point of view, yet it has not received a satisfactory experimental realization. Other authors have proposed to create field-resilient superconducting devices by engraving protective flux moats [22–24] which could also be fabricated by means of anisotropic frames surrounding the protected area. Finally, related to the extensively investigated interaction between superconducting vortices and other topological objects such as magnetic skyrmions [25], one may find proposals of using fluxon lattices as templates for imprinting skyrmions in neighboring layers [26], as well as controlling the motion of such skyrmions [27]. Again, the control of magnetic flux pathways through anisotropic surface structures in the superconductor could act as a mask to control the neighboring skyrmion dynamics.

An emerging technique to produce nanopatterns and other surface modifications is based on the irradiation with femtosecond (fs) pulse lasers. This method, of growing interest in recent years, has already been applied to achieve performance improvements of very diverse thin films by inducing chemical, structural, and/or physical modifications [28–33]. Related to this, in previous works [34,35], it was shown that surface nanostructures can modify the superconducting properties of Nb sheets, and we conceived the functionalization of Nb thin films by fabricating anisotropic surface topographies devised as rails for the magnetic flux [36]. We showed that surface nanopatterning by ultrashort pulsed-laser irradiation may result in anisotropic electromagnetic behavior for superconducting Nb films. More specifically, by selecting adequate conditions, laser-induced periodic surface structures (LIPSS), also named ripples, can be generated on the sample's surface. The current carrying capacity of Nb films is enhanced along the direction of thereby induced quasi-parallel ripples. As a matter of fact, by properly assembling conjoined domains of ripple structures, we could demonstrate the possibility of building flux pathways in the films [37]. Nevertheless, together with this appealing property, it was noticed that the intrinsic nature of the underlying superconducting material may be undermined. In particular, a faint reduction of T_c was reported [37], suggesting a correlation with the microstructural modifications induced by laser irradiation. Thus, in samples with a non-homogeneous laser-patterning motif, magneto-optical imaging (MOI) experiments revealed a locally changing value of T_c for zones with different microscopic order.

In this work, we present an oriented investigation of phenomenology related to the formation of LIPSS in Nb thin films. Special emphasis is placed on the ability to control the surface modifications induced by the laser pulses, as well as the implications for the performance of the superconductor. Furthermore, focusing on the relevance of patterning in the mesoscopic scale (motif size Λ is comparable to the typical lengths of superconductivity ξ, λ for Nb), we have performed time-dependent Ginzburg–Landau (TDGL) simulations that support our interpretation of the underlying physics in the samples with surface undulations.

The article is organized as follows. In Section 2, we give details on the sample fabrication and laser patterning methods, as well as about the experimental characterization techniques (SEM, TEM, AFM, XRD, SQUID magnetometry, and MOI). Section 3 presents the main findings, showing the most relevant microstructural (lattice parameters, surface topography) and physical properties (critical fields, currents, and temperatures) of the irradiated films as compared to the pristine samples. Finally, in view of the observed phenomenology, TDGL simulations are compared with experimental results to extract some insights on the influence of laser-processing techniques on the superconducting properties. Summarizing conclusions are given in Section 4.

Table 1
Description of the two types of samples used in this study (square film and bridge samples) and laser pulse energies used for surface nanopatterning. The other (shared) laser irradiation parameters are given in the text.

Sample name	Description	Pulse energy E_p(μJ)	E_p/E_{LIPSS}
FS0	Square, pristine	0	0
FSj	Square samples ($j = 1, 2, 3, \dots$)	1.2 – 3.8	0.35 – 1.10
FSL	Square, fully covered by LIPSS	3.4	1
BS0	Bridge, pristine	0	0
BS_{PAR}	Bridge, parallel LIPSS	3.4	1
BS_{PERP}	Bridge, perpendicular LIPSS	3.4	1

2. Materials and methods

2.1. Sample fabrication and laser nanopatterning

Nb thin films ($d \approx 190$ nm of thickness) were deposited onto Si/SiO_2 wafers, using radio-frequency magnetron sputtering. The Nb physical vapor deposition was conducted at a rate of 0.1 nm/s under an Ar pressure of 5 mTorr, after pumping down the chamber to a base pressure of $4 \cdot 10^{-8}$ Torr. The resulting Nb films have a RMS roughness Sq ≈ 1.8 nm and are composed of small grains (of about 20–30 nm in size) disposed in columnar arrangement [37].

A pulsed laser (Light Conversion, Vilnius, Lithuania, model Carbide CB3-40 W) was used for cutting, ablating, and nanopatterning the samples, as described below:

(i) *Sample cutting*: To begin with, square samples were laser-cut from the wafers using wavelength $\lambda = 515$ nm, pulse width $\tau_p = 249$ fs, pulse repetition frequency $f_{rep} = 10$ kHz and a laser scanning speed $v = 5$ mm/s. After the machining process, the samples were ultrasound cleaned in isopropanol for 15 min.

Two types of samples were prepared in this study, which will be named after "film" and "bridge" (see Fig. 1 and Table 1). The former are square-shaped samples, whereas the latter are dedicated geometries for resistive measurements.

(ii) *Fabrication of bridges*: As sketched in Fig. 1B1, the bridges have reduced widths, W, of a few tens of microns and were fabricated from the square samples by complete removal of the Nb layer on selected areas using the following conditions for laser ablation: $\lambda = 343$ nm, $\tau_p = 238$ fs, $f_{rep} = 20$ kHz, $v = 125$ mm/s, distance between lines $\delta_l = 6$ μm and pulse energy $E_p \approx 6.0$ μJ.

As it will be later discussed, the bridge geometry conveys several advantages: (a) a lower level of transport current is needed, (b) the analysis of experiments is simplified (the orientation of the current density vector **J** is known *a priori*) and (c) one gets rid of extrinsic spurious effects, concomitant of anisotropic 2D configurations (see Supplementary material).

(iii) *Surface nanopatterning*: Finally, as also sketched in Figs. 1A and B2, the surface of film and bridge samples was nanopatterned to produce LIPSS by laser scanning the sample using the following parameters: $\lambda = 343$ nm, $\tau_p = 238$ fs, $f_{rep} = 20$ kHz, $v = 125$ mm/s, $\delta_l = 8$ μm and $E_p = E_{LIPSS} \approx 3.4$ μJ as the pulse energy. For the selected wavelength and at the established working distance, our laser beam exhibited a spatially Gaussian energy profile with an elliptical spot of semi-axes 18×30 μm^2 for the $1/e^2$ decay distance. This set of laser-irradiation parameters, critical for the generation of uniform LIPSS structures, was refined on a previous study [37].

Two bridge samples were irradiated to generate LIPSS either parallel or perpendicular to the path between voltage pads (i.e., parallel or perpendicular to the current applied in transport measurements). In addition, we irradiated a series of square samples (of width $2b \approx 3$ or 4 mm) with varying E_p values ranging from 0.35 to 1.1 E_{LIPSS} (the rest of laser conditions remaining unchanged). In all cases, a controlled Ar atmosphere (gas flow in an open chamber) was used, not only for reducing possible oxidation induced by laser-processing in air, but also as a means of removing debris particles through the gas flow.

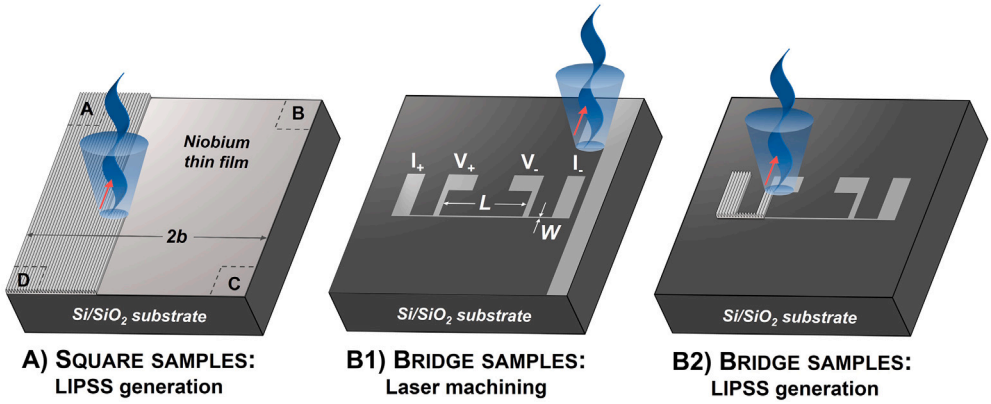

Fig. 1. Sketch of sample geometries and laser scanning processes: (A) 2b × 2b square films were irradiated with a fs UV laser using different E_p values for surface nanopatterning. (B1) The Nb layer was selectively removed by laser ablation to define a transport bridge geometry. (B2) Subsequently, the surface was corrugated by laser irradiation ($E_p =$ 3.4 μJ). For resistive measurements, ultrasonic wire bonding was performed on the four corners (A–D) for the square films or on top of the specific pads ($V_{\pm}, I_{\pm}$) for the bridges. For visual purposes, the laser spot is not to scale.

2.2. Microstructural observations

2.2.1. Electron microscopy

Surface characterization was carried out using a MERLIN field-emission scanning electron microscope (FE-SEM) (Carl Zeiss in Jena, Germany), equipped with an energy dispersive X-ray spectroscopy (EDS) system from Oxford Instruments (Abingdon, UK). The FE-SEM was operated at 5 kV and utilized secondary electron (SE), in-lens, and energy-selective backscattered (ESB) detectors. Cross-sectional TEM images were taken with a Tecnai F30 microscope of FEI (Lincoln, NE, USA). With this aim, several lamellas were prepared using a Focused Ion Beam (FIB) in a Dual Beam Helios 650 apparatus of FEI. Prior to the FIB-lamella extraction, samples were coated with C-Pt protective layers.

2.2.2. Atomic force microscopy (AFM)

AFM profiles of selected square film samples irradiated with different E_p values were performed using a Drive Nanosurf AFM. This system is equipped with super-sharp silicon tips (SSS-NCHR from Nanoworld) characterized by a typical curvature radius of 2 nm and a spring constant of 42 N/m. Measurements were conducted in tapping mode at a driven frequency of 275 kHz. Surface roughness was assessed by averaging multiple measurements over 5 × 5 μm^2 areas at various locations in the sample. Data processing was carried out using the open-source software Gwyddion.

2.2.3. X-ray diffraction

X-ray diffraction (XRD) analyses were conducted on a series of thin films irradiated with different pulse laser energies in order to assess the influence of the radiation on the material's crystal structure. Measurements were performed using a PANalytical Empyrean system configured in Bragg–Brentano geometry, equipped with a copper anode X-ray source ($\lambda =$ 1.5418 Å) and a PIXcel linear detector covering an angular range of 3.3°. To collect the complete signal from the film within the 30–45° detector angle range while avoiding the strong reflection from the single-crystal silicon substrate at $2\theta =$ 66.2°, the incidence angle (ω) was deliberately tilted by 5° away from the symmetric position. Data processing included curve smoothing by removing the background and averaging the measured values over every 10 data points to minimize errors in the resulting curves.

The lattice parameter a of the body-centered cubic Nb [38] was calculated for each sample from the diffraction measurements. As customary, we used Bragg's law to determine the interplanar spacing $d_{hkl} = n \cdot \lambda / 2 \sin\theta$, i.e.: $a = d_{hkl} \cdot \sqrt{h^2 + k^2 + l^2}$ with $n = 1$ (first-order diffraction), λ the X-ray wavelength, θ the diffraction angle; and h, k, l the Miller indices of the plane, in this case (110).

2.3. Electromagnetic measurements

Electric transport and inductive measurements were performed in our thin films, focused on the influence of the laser-induced modifications on their physical properties.

2.3.1. Electrical resistivity

The electrical resistivity of bridges and square films was measured from 3 K to room temperature in a Quantum Design PPMS instrument (San Diego, CA, USA) with DC field (0 to 1 T) applied perpendicular to the film's surface. For the case of square films, a standard van der Pauw configuration was used. Taking advantage of the multichannel options, the experimental data were obtained simultaneously for three different samples subject to comparison. In particular, we measured $\rho(H)$ for different sets of temperatures as well as $\rho(T)$ for sets of values of the applied magnetic field. In between each set of measurements, the samples were heated above the superconducting critical temperature and allowed to cool down in a zero magnetic field. The T_c values of the samples were obtained from $\rho(T)$ at zero DC field, while the higher critical fields were derived from the transitions in terms of the applied field at different temperatures $\rho(H, T_0)$.

2.3.2. SQUID magnetometry

The complex AC susceptibility, $\chi_{ac}(T)$, with in-phase χ' and out-of-phase χ'' components, was measured at zero DC magnetic field and AC drive magnetic field (sine wave amplitude $\mu_0 h_0 = 10$ μT, frequency $f = 10$ Hz) in a SQUID magnetometer (MPMS3 from Quantum Design, San Diego, CA, USA). The T_c values of the square film samples were obtained from these measurements using the onset of diamagnetism criterion. The same system was used to perform hysteresis loops $M(H)$ at constant temperature using a scan length of 3 cm. The magnetic field was ramped at 2 mT/s to each set value with the non-overshoot mode. After field stabilization, the system was paused for 2 s before the measurement started.

All magnetic measurements were performed on the above-described square samples with the magnetic field applied perpendicular to the surface and after zero field cooling. For each measurement, a reset of the superconducting magnet was performed previous to sample cooling in order to minimize its remnant magnetic field.

2.3.3. Magneto-optical imaging (MOI)

The analysis of the magnetic flux penetration in the laser-patterned samples was performed using the magneto-optical Faraday imaging technique. The employed experimental configuration mimics a commercial polarization microscope. A light beam emitted by an LED

lamp passed through a green filter (550 nm) and a linear polarizer before reaching a Faraday active indicator. The indicator in this study consisted of a 3.5 μm-thick layer of Bi:YIG, epitaxially grown on a 450 μm-thick $Gd_3Ga_5O_{12}$ (GGG) transparent substrate, with a 100 nm-thick Al mirror deposited on the optically active layer to ensure adequate reflection of the incident light. The linearly polarized light traversed the GGG substrate and the Bi:YIG layer within the indicator, undergoing a polarization direction rotation corresponding to the local magnetic field. Subsequently, the light was reflected by the mirror, retraced its path through the indicator and the objective, and finally reached an analyzer. The collected light was then directed to a high-resolution CCD camera situated atop the microscope unit, producing an image in which the intensity contrast directly represented the magnetic field distribution. More technical details may be found elsewhere [39].

2.4. Modeling: TDGL theory

To theoretically corroborate the interpretation of our experimental results, we resorted to time-dependent Ginzburg–Landau simulations. This allows us to obtain the flux vortex dynamics in samples with arbitrary motifs at the mesoscopic scale, a circumstance that matches our situation, i.e., with corrugations of size similar to the fundamental superconducting parameters (coherence length ξ and penetration depth λ) for Nb in the experimental range.

In brief, one may derive the maximum (critical) current density J_c in the superconducting state by determining the threshold for the appearance of magnetic flux depinning under specifically imposed boundary conditions. In particular, we have investigated the differences between submitting current either along or across the LIPSS. Focusing on this, we have quantified the expected enhancement for the configuration in which vortices are driven across the surface undulations. The simulations were carried out through the numerical solution of the two-dimensional TDGL equation adapted to our Nb superconducting films with variable thickness [40]. Specific details on the actual mathematical procedures are given in Appendix A.

3. Results and discussion

Some fundamental questions have been focused, aiming at the elucidation of the correlation between the laser-processing parameters and the evolution of the microstructural and physical properties.

3.1. Laser patterning: evolution of the microstructure

The gradual effect on the topography and microstructure of the Nb films upon increasing the laser pulse energy may be recognized in Fig. 2. According to the AFM data, and starting from the pristine sample FS0, we first observed a slight increase in surface roughness up to 6.6 nm for the sample irradiated with $E_p/E_{LIPSS} = 0.58$. Upon increasing this factor to about 0.7, LIPSS start nucleating non homogeneously at first, as seen in Fig. 2C, corresponding to $E_p/E_{LIPSS} = 0.78$, where the characteristic peak-to-valley amplitude, $d_{peak\text{-}valley}$, reaches a value of 50 ± 15 nm (Sq = 12.8 nm). The LIPSS progressively reach homogeneity, as shown in Fig. 2D ($E_p = E_{LIPSS}$), where complete surface coverage is observed, with $d_{peak\text{-}valley} = 70 \pm 20$ nm and Sq = 18.5 nm. Upon further increasing E_p by about 10%, small holes begin to appear in the Nb films.

The 2D Fast Fourier Transform (2D-FFT) analysis of the SEM images shows that once formed, ripples have a similar spatial period $\Lambda = 260 \pm 5$ nm and are aligned perpendicular to the laser polarization direction. Note that the sample represented in Fig. 2B already exhibits slight preferential (bidirectional) organization as revealed by the 2D-FFT, unlike the pristine sample. TEM images of the cross-sections of the same samples also display some gradual changes, such as a specific decrease in the film thickness, the gradual formation of the undulated structure, as well as an increase in the grain size, especially at the top of the LIPSS, upon increasing pulse energy values. In order to assess these observations as an overall property of the samples' microstructure, we provide complementary images across larger areas in the Supplementary Material. The degree of order of the obtained "quasi-parallel" structures, which is visible in Fig. 2, is also quantified in the Supplementary section. On average, an angular dispersion around the direction perpendicular to the laser polarization of $\approx \pm 18°$ is obtained in our optimized structures. Here, it is worthy to mention that highly ordered gratings of LIPSS ($\approx \pm 5°$ over areas above tens of μm^2) have been recently reported for Hf and Au thin films [41,42] under proper irradiation conditions. However, and most probably related to the complex kinetics of the LIPSS formation process, the generation of such homogeneous structures appears related to perforation of the film. This condition is unacceptable for the applications envisaged here, and, for this reason, our optimization process ends up with a moderate degree of order, just before holes start appearing.

SEM images of the surfaces of the bridge samples are displayed in Fig. 3. The images were taken in the area between voltage pads (green rectangle in this figure). At the center of the pristine bridge BS0, some small particles are visible on the surface, probably generated during the machining process. Note also that unsought LIPSS are generated during the Nb layer removal around the path in this sample, as related to the laser beam lateral tails (gaussian energy distribution of the laser spot [36]), having a total width of approximately 12 ± 2 μm (about 8 μm of connected LIPSS and 4 μm with disperse LIPSS, without percolative paths). At the center of the paths of the BS_{PAR} and BS_{PERP} samples, LIPSS are similar to those of the FSL sample but with two different orientations, eventually parallel or perpendicular to the applied current, which will flow along the horizontal direction in these images. In both samples and for the same reason as above, there is an area around the paths' edges where the LIPSS are more pronounced, producing many holes in the Nb layer. Because the local current there (in a strip of width of about 4–8 μm) will be negligible, these zones were not taken into account to estimate the path width, $W \approx$ 53, 25 and 37 μm for BS0, BS_{PAR} and BS_{PERP}, respectively, with estimated error of $\approx \pm 2$ μm. Note the larger width of sample BS0 in order to minimize the effect of the mentioned LIPSS formed at the edges, and the arrangements of the boundary LIPSS for the samples BS_{PAR} and BS_{PERP}, deliberately along the same direction of the central ones.

XRD experiments were conducted for a set of square film samples irradiated with different laser pulse energies in order to analyze the effects on the film's crystallographic properties. Fig. 4A displays a gradual shift of the Nb (110) diffraction peak angle upon increasing pulse energy values. Thus, for the non-irradiated samples, this peak is at $2\theta = 38.5°$, which corresponds approximately to the value for bulk cubic (Im3m) Nb [38], and shifts to $\approx 39.0°$ for $E_p = E_{LIPSS}$ (FSL sample). Correspondingly, the estimated lattice parameter for the pristine sample FS0 is 3.3055 ± 0.001 Å, and decreases upon increasing the pulse energy increases, first smoothly for $E_p/E_{LIPSS} < 0.6$, and then more sharply from $E_p/E_{LIPSS} \approx 0.7$, coincident with the initial generation of LIPSS on the film surface (see Fig. 4B). It is noted that the lattice shrinkage for the sample fully covered by LIPSS (FSL, $E_p/E_{LIPSS} = 1$) is thus $\approx 1.05\%$ as compared to the pristine sample. Finally, note that there is a noticeable decrease of the diffraction peak height intensity for the sample irradiated with $E_p/E_{LIPSS} = 1.1$. It occurs in parallel with the appearance of holes in the Nb film for this sample.

3.2. Intrinsic superconducting parameters

Critical temperature T_c. The critical temperatures of the analyzed samples were obtained from AC susceptibility and resistivity measurements under zero DC magnetic field. Fig. 4C shows the superconducting-to-normal transition observed in $\chi'(T)$ of selected square film samples. This transition shifts towards lower temperatures upon increasing E_p, but its width, ΔT, defined here as the temperature interval where χ'

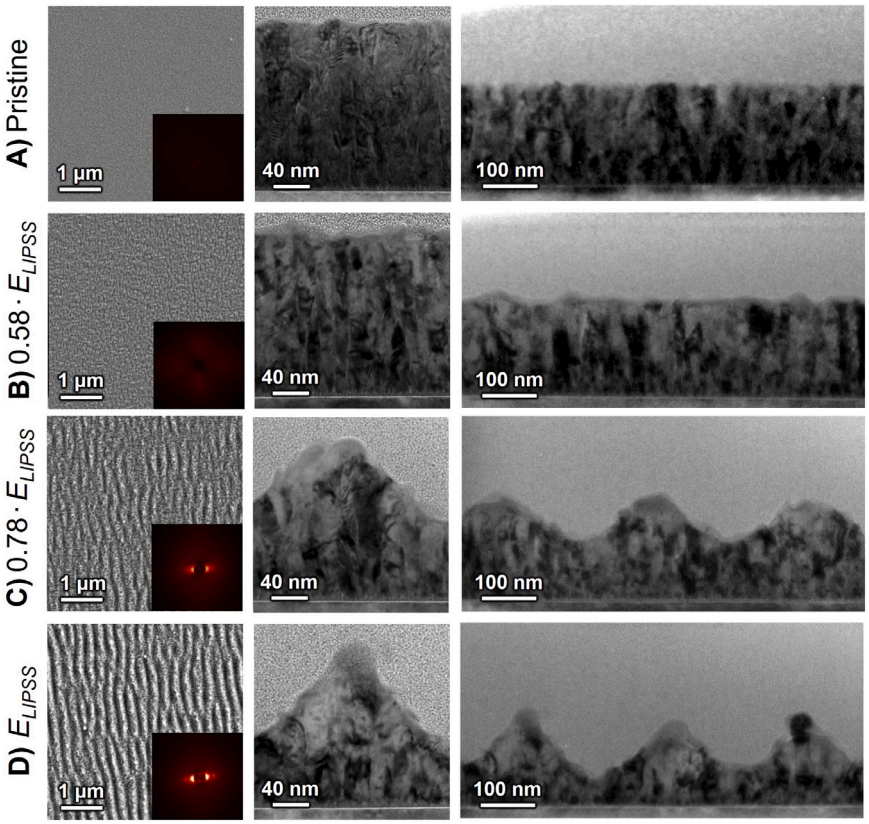

Fig. 2. Microstructural details of square-shaped samples that show the gradual effect of increasing the laser pulse energy. (A) Pristine sample (FS0); (B) and (C) two samples of the series FSj irradiated with two intermediate E_p values as indicated; and (D) Sample FSL whose surface is fully covered by LIPSS. Left panels: Top-view SEM (SE) images. Insets show 2D-FFT of SEM images (≈ 70 μm^2 of area). Middle and right panels: Cross-sectional brightfield TEM images.

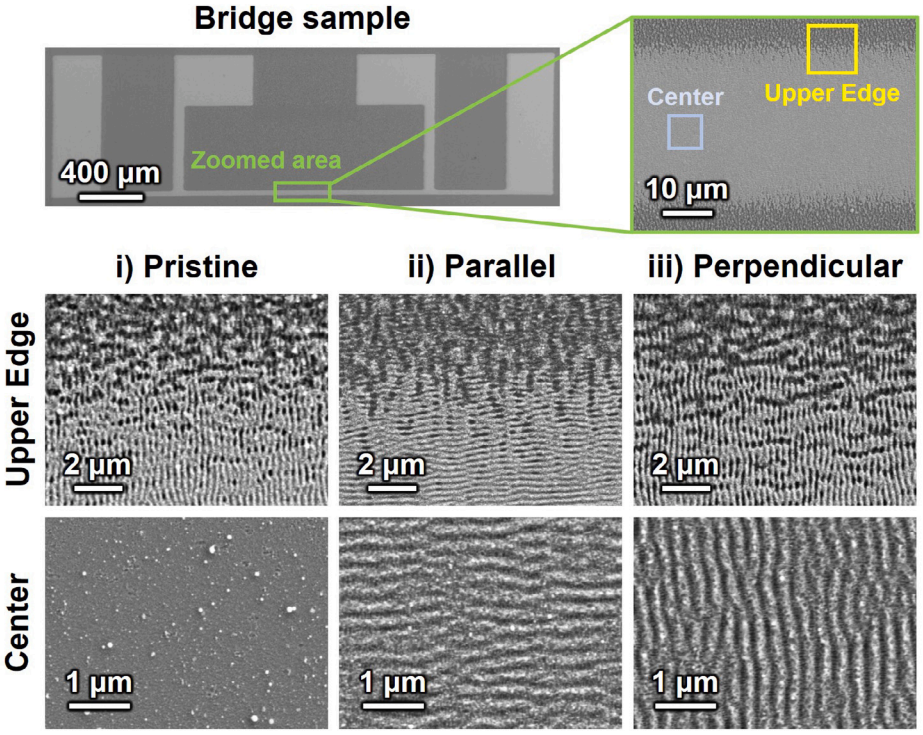

Fig. 3. SEM (SE) images of the surface of bridge samples: the upper panels correspond to the sample BS_{PAR} and show the complete circuit and a detail of the bridge between the voltage contacts. Middle and lower panels show details at higher magnification of the bridges near the center and at the edge for the three analyzed samples: BS0 (pristine), BS_{PAR} (parallel), and BS_{PERP} (perpendicular). The unwanted laser-patterning induced LIPSS of the pristine sample (BS0) occupy a lateral strip of 12 ± 2 μm (see text).

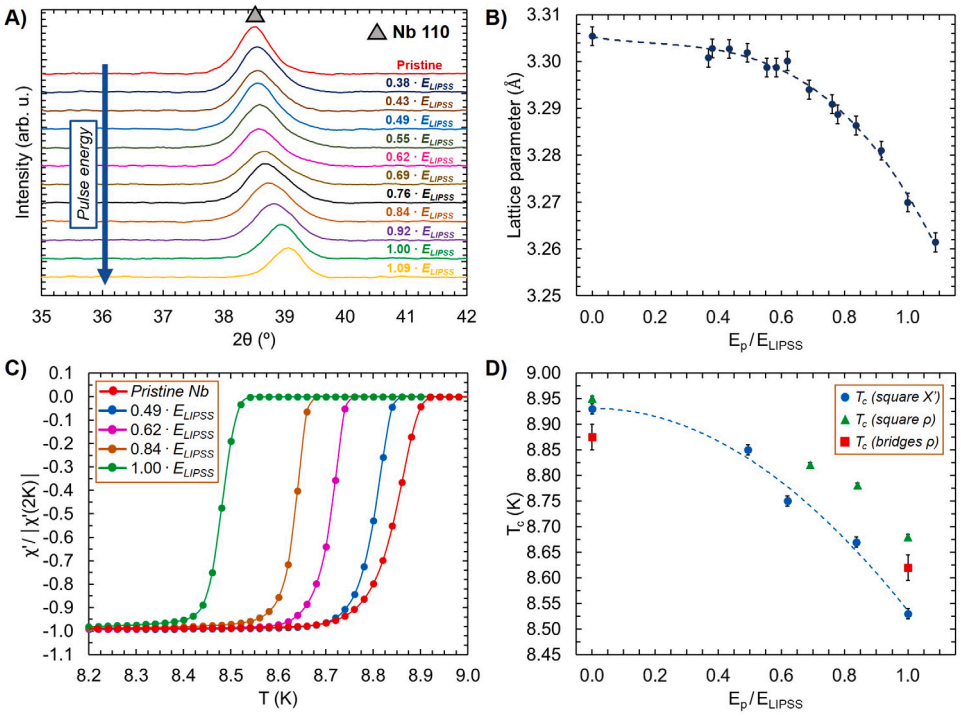

Fig. 4. Effect of changing the laser pulse energies: (A) (110) diffraction peak of Nb. (B) Estimated lattice parameter a from the XRD experiments. (C) $\chi'(T)$ scaled by $|\chi'(2K)|$, showing the superconducting-to-normal transition at zero DC field of square films processed with different pulse energies. (D) T_c values estimated from susceptibility or resistivity measurements of several bridge and square samples, as indicated. Reference values for bulk Nb (not displayed): $a = 3.3066(1)$ Å [38], $T_c = 9.25 \pm 0.01$ K [43]. Dashed lines are guides for the eye.

changes between 0.05 to 0.95 of the signal measured at 2 K, does not vary significantly among the samples (≈ 0.11–0.18 K). In the figure, $\chi'(T)$ is scaled by $|\chi'(2K)|$, which is close to the value expected for perfect diamagnetism in perpendicular fields, $\chi'_{\text{ideal}} = 0.9\ b/d$ [44]. T_c estimated from these measurements decreases from 8.93 K in our pristine films down to 8.53 K for $E_p = E_{\text{LIPSS}}$, as displayed in Fig. 4D. The same trend is also found for the T_c values obtained from resistivity measurements in square and bridge samples, also represented in the figure for comparison purposes. In this case, the transition widths were $\approx 0.02 - 0.05$ K. The differences among datasets are likely due to the different conditions applied in each experiment: the used applied AC field amplitude ($\mu_0 h_0 = 0.01$ μT for the square samples) and transport currents (1 μA for bridge samples and 100 μA for square samples), as well as to the fact that measurements are done in different instruments. Nonetheless, some general trends may be extracted. Note, for instance, that both bridge samples with LIPSS have the same critical temperature. Note also the similarity between the functions depicted in Fig. 4B and Fig. 4D, suggesting a correlation between both variables, a and T_c. This is in agreement with previous results [3] in which decreasing trends of T_c were observed in Nb films with increasing compressive and tensile strains (with stronger dependence for the latter). One may conclude that approaching E_{LIPSS}, the crystal lattice parameter decreases. This implies a compressive stress which in turn leads to a decrease of T_c.

Primary experimental data for the determination of T_c from the resistive measurements are provided in the supplemental material section. $\rho(H,T)$ curves were measured in a range of fields and temperatures for films and bridges.

Critical field H_{c2}. Based on the $\rho(H,T)$ measurements, complementary information on the reduction of the critical temperature is provided in the supplemental section. In particular, based on the reduction of the transition temperature under an applied magnetic field, we provide the $H_{c2}(T)$ phase diagram, that also displays the reduction of the critical field related to the laser irradiation process.

In general, we may summarize that the equilibrium properties of our laser-treated samples (T_c, H_{c2}) are basically independent of the current density orientation relative to the LIPSS, while always (slightly) depressed as compared to the pristine sample, i.e.: the resistance curves for the laser-treated samples are always shifted to lower fields and temperatures relative to the nearly coincident curves for the samples with LIPSS. Specifically, this reduction is characterized by the values $\Delta T_c \approx 0.3$ K and $\Delta H_{c2} \approx 50$ mT for films with fully formed LIPSS, and occurs isotropically.

3.3. Flux pinning landscape

In the previous sections, we have dealt with the laser-induced variations of the intrinsic superconducting properties of Nb (T_c, H_{c2}). According to our observations, changes are systematic in terms of the laser pulse energy, and faintly dependent on the measurement configuration. In particular, differences related to the circulation of the transport current either parallel or perpendicular to the LIPSS (anisotropy) are hardly visible. Below, we will concentrate on the influence of laser irradiation in the (extrinsic) flux-pinning landscape. In particular, we will show that the behavior of the samples becomes anisotropic and also much sensitive to the experimental conditions (applied field and temperature). This study was performed at temperatures $T \geq 6$ K, in order to minimize the occurrence of magnetic flux avalanches, a detrimental phenomenon ubiquitous in films at low temperatures [45], already investigated in Nb samples in our previous work [36].

3.3.1. Irreversible magnetization. Inductive J_c

As it is customary for type-II superconductors, we have analyzed the hysteretic magnetic response of the samples based on the isothermal $M(H)$ loops. Considering that the thicknesses of the samples d are affected by uncertainty (Fig. 2), we have preferred to evaluate the sheet current for each case, i.e., $K_c \equiv J_c d$. Note that the corresponding

(approximate) J_c values are also displayed to ease comparison with literature. Recall that, according to critical state model (CSM) predictions, the induced critical current density is proportional to the width of hysteresis loops, Δm, which is obtained at each value of the applied field as the difference between the measured magnetic moments of descending ($m_\downarrow$) and ascending ($m_\uparrow$) field branches ($\Delta m = m_\downarrow - m_\uparrow$). For isotropic hard superconductors of square cross-section $2b \times 2b$ in longitudinal field, this is given by [46,47]:

$$K_c = \frac{3}{8}\frac{\Delta m}{b^3}\,; \qquad J_c = \frac{3}{8}\frac{\Delta m}{b^3 d} = \frac{3}{2}\frac{\Delta M}{b}\,. \tag{1}$$

Here, we have introduced the sample's magnetization $\Delta M = \Delta m/V$, V the volume. We note that the above analytical expression was obtained for superconductors with infinitely long geometry ($d \gg b$) and field applied parallel to the axis. Still, it is also generally valid for finite length when both branches are in fully penetrated states. In fact, it is important to recall that due to shape effects, the intrinsic $J_c(B)$ can be obtained from the width of the magnetization loop with the greatest accuracy in the case of thin films ($d \ll b$) with the field applied parallel to the shortest dimension [48], as in this study (square thin films lying in the xy–plane with field applied along z-axis). Essentially, one may safely approximate $B \approx \mu_0 H$, i.e., self-field may be neglected.

Fig. 5 displays the induced K_c and J_c as a function of $\mu_0 H$ at 6, 7 and 8 K for the same square-shape films of Fig. 4C, as obtained by application of Eq. (1). These values were estimated from the third and fourth branches of the magnetization loops of the different samples, instead of using the first (initial) and second ones, so that the applied field fully penetrates the sample. In general, J_c exhibits a temperature-dependent initial strong decay in the range $\mu_0 H < 10 - 30$ mT, followed by a smoother decay or "plateau" and eventually a larger decay rate at higher fields. It must be remarked that the effect of laser irradiation with conditions below the threshold for the formation of LIPSS ($E_p/E_{LIPSS} < 0.7$) is just a small but progressive increase of J_c upon increasing laser pulse energy, being all these $J_c(\mu_0 H)$ curves very similar. On the contrary, once LIPSS start nucleating, strong variations on $J_c(\mu_0 H)$ are observed. Thus, compared to FS0, these samples show substantial improvements of J_c at low fields ($\mu_0 H < 20$–40 mT), mainly at 6 K and 7 K, whereas the opposite occurs at the highest fields.

As concerns the origin of the increased J_c, a simplified interpretation was done in previous work [36] by assuming a laser-induced anisotropy. Thus, according to the expression of the modified magnetization [36,49]:

$$M_{aniso} = M_{iso}\frac{3 - 1/\Gamma}{2}\,, \tag{2}$$

one may expect a growth of the saturation magnetic moment for the anisotropic (field-independent) case when the critical current density increases along the x-axis, while remaining as in the isotropic case in the y-axis (i.e. $J_{cx} = \Gamma J_{cy}$, with $\Gamma > 1$ for the sample lying on the xy–plane and magnetic field applied along z-axis).

In passing, we note that a further argument aligned with the interpretation of our results in terms of anisotropy is the observation of bumps in the field dependence of the critical current density, which may be attributed to the appearance of flux-matching effects in the presence of a periodic potential related to the undulated topography of the sample [50]. In fact, using the expression $H_1 \approx (\sqrt{3}/2)\Phi_0 \Lambda^2$ with Λ the periodicity of the LIPSS structure mentioned before, one gets $H_1 \approx 26.52$ mT in good agreement with the observed bumps in Fig. 5.

It must be stressed that the above considerations are just a *first approach* to the full problem. In particular, the relevance of the field dependence of J_c is masked by and mixed with the coexistence of current densities along the two anisotropy directions in the experiment. To remove ambiguity, we also performed transport measurements (Section 3.3.2) in the bridge geometry so as to separate both effects.

Notwithstanding the above, the information provided by magnetization loops is very useful as it allows for analysis of the effect on the hysteretic behavior of gradually increasing the laser irradiation energy. Moreover, it gives access to the range of high current densities ($\sim 5 \cdot 10^8 - 1 \cdot 10^9$ A/m^2), above the experimental scope in our transport measurements.

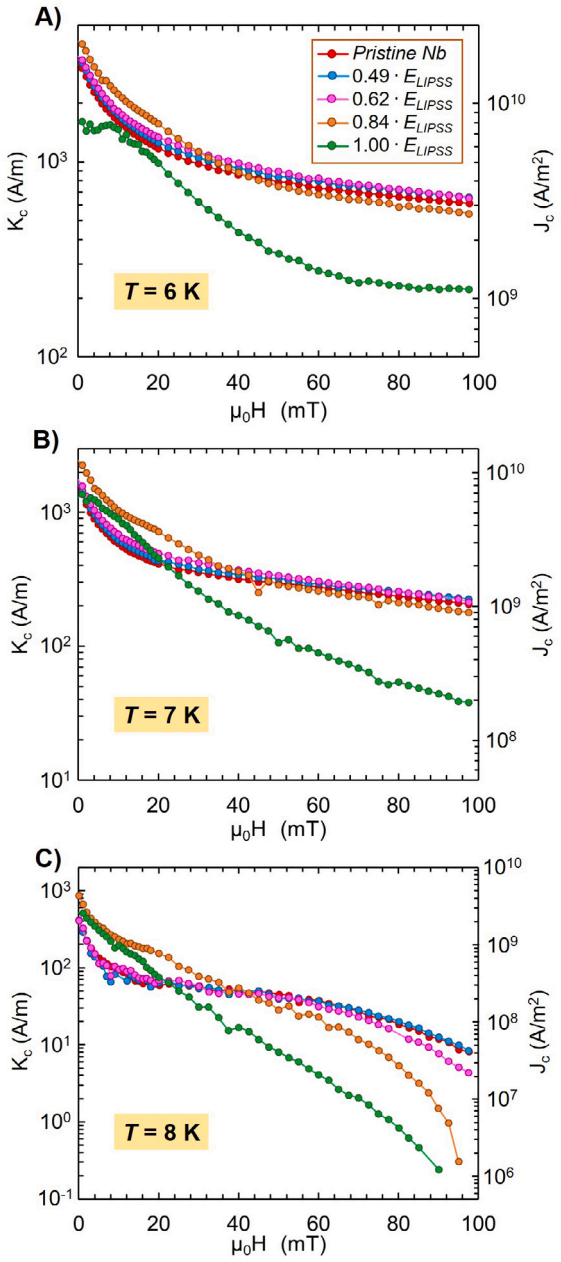

Fig. 5. Field dependence of the inductive critical currents (Eq. (1)) at different temperatures: (A) $T = 6$ K, (B) $T = 7$ K and (C) $T = 8$ K, for the square films under different irradiation conditions. The same samples (and color code) as in Fig. 4C are used here.

3.3.2. Anisotropic transport critical current density

To better establish the correlation between the physical properties with the circulation of currents along or transverse to the LIPSS, we measured the electrical resistivity of the three bridge samples (Fig. 3) for different applied transport currents. The use of high enough current densities gives insight into the flux depinning dynamics, and thus, on the underlying pinning structures (recall the expression $\mathbf{F} = \mathbf{J} \times \mathbf{B}$ for the unit-volume depinning force). Primary experimental data, i.e., resistance curves for different values of the applied current, magnetic field,

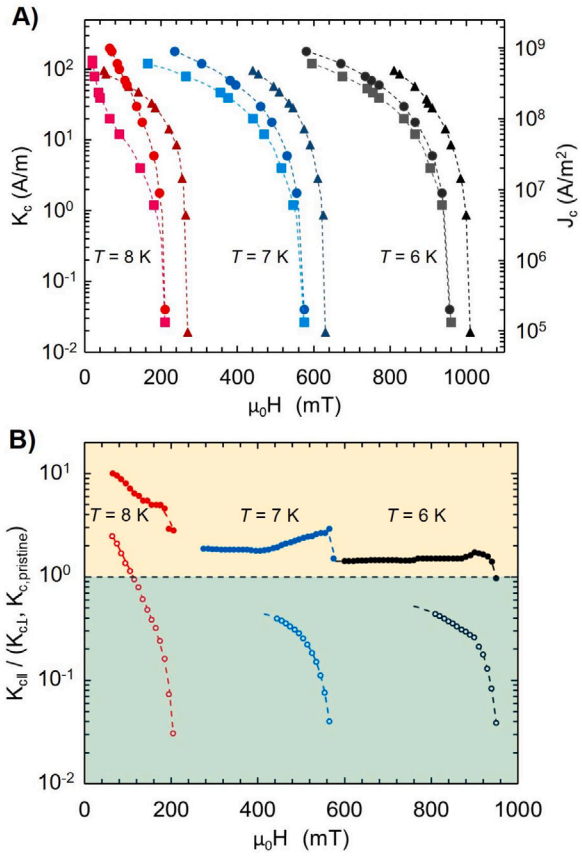

Fig. 6. (A) Critical sheet currents ($K_c \equiv I_c/W$) obtained from transport measurements for the pristine and laser-treated samples. Triangles correspond to the untreated Nb bridge ($K_{c,pristine}$), circles are for the parallel configuration bridge ($K_{c\|}$), and squares for the perpendicular configuration ($K_{c\perp}$). (B) Field dependence of the anisotropy ratios $K_{c\|}/K_{c\perp}$ (full symbols) and $K_{c\|}/K_{c,pristine}$ (open symbols) of the transport critical sheet currents obtained for the "parallel", "perpendicular" and "pristine" bridge configurations at the temperatures of 6, 7 and 8 K. The horizontal line (unit ratio) separates the regimes for which the laser treatment either improves or deteriorates the transport properties of the films, i.e., $K_{c\|} \gtrless K_{c,pristine}$.

and temperature, additional explanations related to the aftermath of anisotropy in the analysis of transport data, as well as the influence of the threshold used to determine the critical current density, are provided in the supplemental material.

In Fig. 6A, the comparison of the critical current densities derived for the two irradiated bridge samples systematically shows higher/lower values of J_c for currents flowing along/across the LIPSS. Also, at each temperature, a tendency to the convergence of both curves for the higher values of the applied field is observed. We notice that this "high-field and low-current limit" of the $J_c(H)$ curves may be identified with H_{c2} for the sample at the given temperature. The convergence of the values for the parallel and perpendicular orientations agrees with the discussion in Section 3.2, i.e., the orientation-independent modification of the superconducting reversible properties by laser-irradiation.

Thus, as H approaches H_{c2} (which corresponds to the measurements for the lowest transport currents in Fig. 6), one may note the downshift in the $H-T$ line as observed in section S1.1 of the supplementary material. On the other hand, at 8 K, a crossover between the curves corresponding to the samples BS0 and BS_{PAR} samples is observed. The irradiated sample BS_{PAR} shows higher performance. Thus, aligned with the observation for the inductive critical currents (Fig. 5), the transport critical current density values of the laser-irradiated samples are higher for the higher-temperature & lower-field regime. Strictly speaking, owing to our experimental limitations, the crossover is observed for the parallel orientation and guessed for the perpendicular case. It is remarkable that the crossover current density values at 8 K derived from both techniques are basically coincident $K_c \approx 60$ A/m. It is apparent, however, that the value of the applied magnetic field at which the crossover occurs in the two measurements differs noticeably. In our view, the reduction of this field for the inductive measurements may be related to the indivisible appearance of the components $K_{c\|}$ and $K_{c\perp}$ in such a case. Finally, we note that the characteristic $J_c(H)$ decay displayed by the inductive critical current densities, i.e., initial sharp drop followed by a smoother rate for higher fields, is also observed in the transport-derived critical current densities.

For further clarity concerning the anisotropic nature of the critical current densities, Fig. 6B displays the current density ratios as a function of the magnetic field at the different temperatures investigated. The plot splits into two regions to highlight the cases for which $K_{c\|}$ surpasses, equals, or is lower than $K_{c\perp}$ or the pristine K_c values. The following tendencies are observed: (i) $K_{c\|}$ and $K_{c\perp}$ display nearly field-independent ratio (> 1) for some ranges of the magnetic field, and (ii) eventually collapse to equality for fields approaching H_{c2}. (iii) The critical current density perpendicular to the LIPSS, $K_{c\perp}$, is generally the lowest, with a tendency (not fully resolved with our data) to exceed the pristine value for their lower field values at the temperature of 8 K. Lastly (iv), we stress that, unless for the highest temperatures and lowest applied fields, the laser-irradiated samples display reduced flux pinning capabilities as indicated by the ratio $K_{c\|}/K_{c,pristine}$.

3.3.3. Anisotropic critical current density from MOI

A dedicated characterization of selected square-shaped films irradiated with different pulse energies was carried out by MOI experiments. This technique allows direct visualization of the anisotropy of J_c in superconductors.

Fig. 7A displays the corners of selected samples obtained by MOI after zero-field cooling the samples to a set temperature and gradually increasing the magnetic field. The temperature and field values in the figure were chosen so as to optimize the visualization and to highlight the differences among samples. For these pictures, the laser polarization in the irradiation process was parallel to the y-axis, so that LIPSS would eventually be generated parallel to the x-axis. Concerning the interpretation of Fig. 7A, we recall that in flat samples subjected to applied magnetic fields in the $z-$direction, the current density streamlines induced in the $x-y$ plane bend sharply, defining the so-called $d-lines$ with a characteristic angle, α, that depends on the anisotropy in the plane [51,52] and is clearly visible in the MOI experiments as dark regions where the screening of the applied field is at its highest. In particular, for the images displayed in Fig. 7A,

$$\tan\alpha = J_{cy}/J_{cx} = J_{c\perp}/J_{c\|} \equiv \frac{1}{\Gamma}\,. \tag{3}$$

As expected, the magnetic flux penetrates isotropically for the pristine film, i.e. $\alpha \approx 45°$. However, as the laser pulse energy increases above approximately $0.60 \cdot E_{LIPSS}$, a sharp decrease in α is observed. Note that this energy corresponds to the onset of LIPSS formation (Fig. 2) and the onset of the lattice parameter reduction (Fig. 4B). More specifically, the angle reduces to about 25° in the sample irradiated with $0.76 \cdot E_{LIPSS}$, and further to 19°, for the sample irradiated at $0.92 \cdot E_{LIPSS}$, with almost fully developed LIPSS.

The variation of the anisotropy parameter Γ obtained by application of Eq. (3) is shown in Fig. 7B. As the corresponding MOI measurements were performed using a full magnetic cycle loop of ±4 mT, one may infer that the observed anisotropic effects emerge already at low fields.

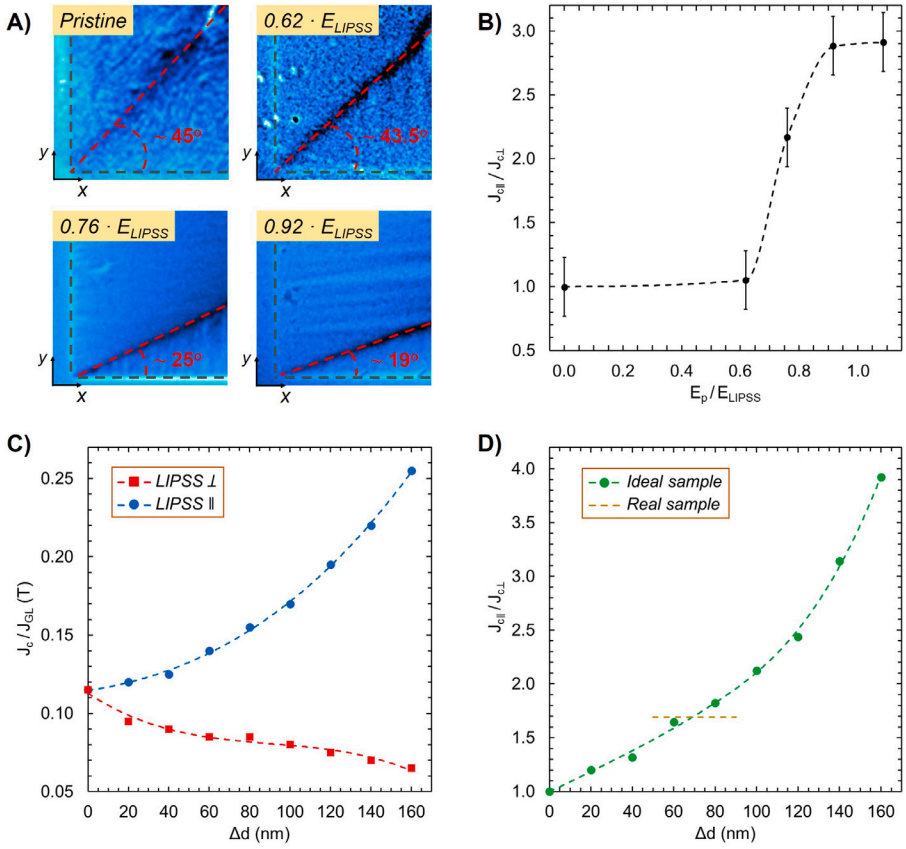

Fig. 7. (A) Magneto-optical images of the corner of the pristine and laser-treated samples with different pulse energies at $T/T_c \approx 0.85$. Dashed gray and red lines highlight the sample's edges and the $d-lines$ (see text), respectively. The average α values, considering all four samples' $d-lines$, are given in each image. (B) $J_{c\parallel}/J_{c\perp}$ ratio obtained from MOI measurements employing Eq. (3), as a function of the relative laser pulse energy, E_p/E_{LIPSS}. The lower panels provide TDGL simulation results: (C) $J_{c\parallel}$ and $J_{c\perp}$ for an ideal undulated thin film of dimensions 5 μm × 5 μm (and thickness 200 nm), in applied field $\mu_0 H = 4$ mT and $T/T_c \approx 0.85$, in terms of the undulation's depth. (D) The anisotropy ratio predicted for the ideal sample, stemming from (C). Dashed lines connecting the symbols are guides for the eye. For comparison, the horizontal dashed line in (D) gives the ratio obtained for the profile of a real sample with $\Delta d = 70 \pm 20$ nm (see text).

3.3.4. *Anisotropic critical current density from TDGL*

Here we put forward the results of our TDGL simulations, targeted to understand the role played by the surface topography on the anisotropy of the critical current density. In fact, as already noticed in early experimental work [50,53–55], based on the concept of *vortex line energy* (free energy per vortex unit length), one may expect that undulations serve to "pin vortices" as they would prefer to sit at the valleys and require energy for hopping across the undulations (which corresponds to the *force* component given by $\boldsymbol{J}_{\parallel} \times \boldsymbol{\Phi}_0$). Also, the deeper the structure, the higher the $J_{c\parallel}$ value as compared to the current necessary to make vortices slide along the valleys ($J_{c\perp}$), going to zero in an ideal crystal. We recall that this intuitive, oversimplified picture neglects realistic effects, such as background pinning, geometric edge barriers and border defects, vortex-vortex interactions, and imperfections in the undulating structure. Nevertheless, as shown below, the monotonic increase of anisotropy with the depth of the grooves is not only an experimental observation, but also a prediction of the TDGL simulations under plausible assumptions, and with reasonable quantitative comparison to experiments. The reader is addressed to the Appendix for technical details on the simulations, which incorporate all the above mentioned effects except for the background pinning.

Fig. 7 (panels C, D) shows the results obtained for an idealized variable thickness profile given by $d(x,y) = d_0 - (\Delta d/2)\left[1 + \cos(2\pi x/L)\right]$, with $d_0 = 200$ nm, $L = 250$ nm, and Δd as a free parameter that determines the depth of the undulation. The values of these parameters mimic the experimental situation in our series of laser-irradiated samples. Also, we show the current density anisotropy obtained for a real thickness profile, as derived from AFM measurements (see Ref. [37]), used as exact $d(x,y)$ input in the simulations. In all simulations, the coherence length is $\xi(T) = 25$ nm, corresponding to operation temperature $T \approx 7.35$ K and critical temperature $T_c = 8.65$ K. For these instances, we take a square superconductor of finite dimensions 5 μm × 5 μm, in an applied field $\mu_0 H = 4$ mT. The critical current densities were defined by the onset of net vortex motion, in this case, also overcoming the barrier at the sample edges. We note that the anisotropy ratio $J_{c\parallel}/J_{c\perp}$ grows as the undulations are made deeper (i.e. with Δd increasing), in reasonable agreement with experimental data. Here, it must be mentioned that, although finite-size effects play a role in the simulations, the predictions of the model were expected to be proper. In fact, as further explained in the Appendix, our simulation platform (5 μm × 5 μm square film) was expected to capture the physics related to the presence of surface topography reasonably, as deduced by testing the model against the infinite geometry situation, completely free from edge barrier effects.

Concerning the plateaus in the experimental curves (Fig. 7B), we note that they are nothing but the thresholds for the nucleation of LIPSS and the eventual perforation of the film, i.e.: within the experimental range of LIPSS formation, as in theory, one has a monotonic increase of anisotropy.

According to the Atomic Force Microscopy studies performed, the statistically averaged depth of undulations for the optimized sample is $\lesssim 80$ nm, which means that the simulations slightly underestimate the experimental anisotropy values (compare panels B and D in Fig. 7). However, considering the assumptions of the model, the quantitative

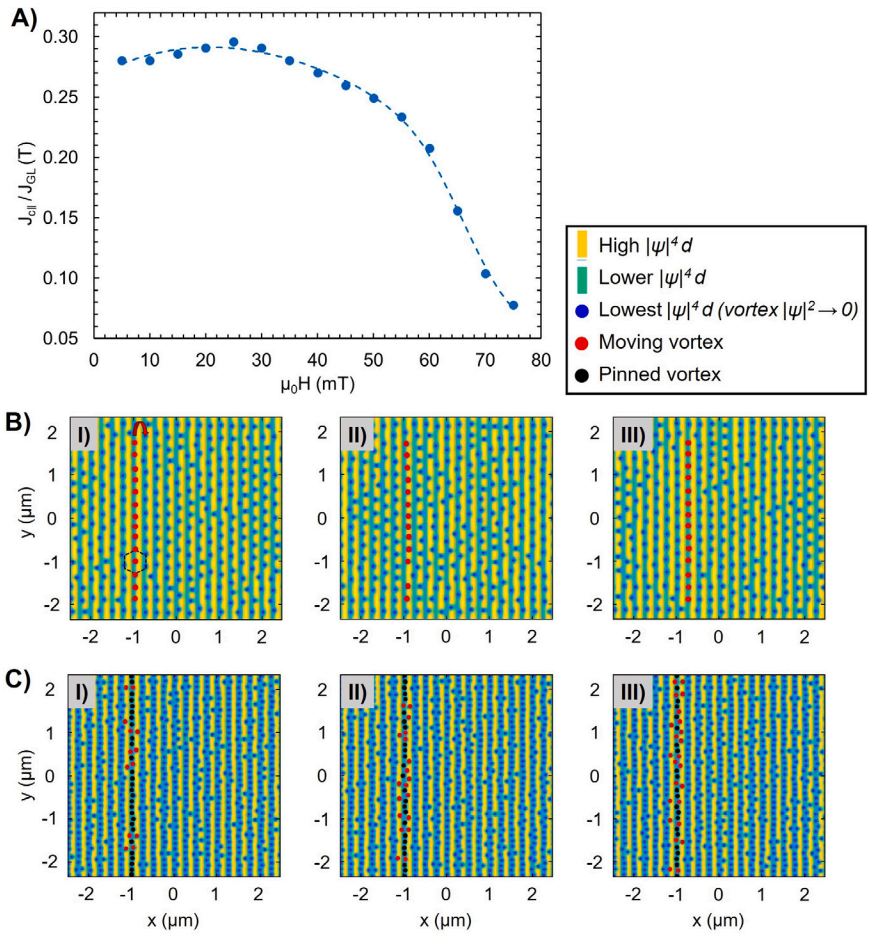

Fig. 8. TDGL simulations for an ideally undulated sample. The upper panel presents $J_{c\|}$ obtained for thickness undulations by Δd = 100 nm, as a function of applied magnetic field in an infinite sample. Dimensionless units are used for J_c in terms of the temperature-dependent Ginzburg–Landau critical current density. The lower panels illustrate some snapshots of the flux dynamics in an undulated film of dimensions 5 μm × 5 μm when a transport current is applied parallel to the LIPSS, for bias fields of $\mu_0 H = 25$ mT and $\mu_0 H = 65$ mT, respectively. A subset of flux vortices is marked in order to outline the different flux flow regimes (see text). Detailed videos are provided at this link for $\mu_0 H = 25$ mT and at this link for $\mu_0 H = 65$ mT.

agreement is noticeable. Related to this, the ideal periodicity ansatz may be considered reliable. In fact, as shown in Fig. 7D, by using the actual AFM scan profile of the reference sample, where the undulations are not ideally periodic, we confirm that the anisotropy ratio is validly determined by the dominating undulation depth ($\approx 70 \pm 20$ nm in the selected region).

The TDGL model provided further physical understanding. To envisage the vortex behavior in the periodically undulated thin film, we fixed the undulations at Δd = 100 nm in our model, and varied the applied magnetic field (i.e., the vortex density). This allows one to comprehend the experimental observation (Fig. 6) of a non-monotonic dependence of the normalized undulation-related contribution to $J_{c\|}$ on magnetic field, increasing at low fields and decreasing at higher fields (see Fig. 8A). Simulations were performed for infinite geometry to disregard other effects than the undulation depth.

For a better visualization of the effect of undulations on vortex motion, we present the color plot of $|\psi|^4 d$ (d is the film's thickness and ψ the order parameter), which can be interpreted as the condensation energy density of the system. In this figure, as well as in the Supplementary Material related animations, maximum (minimum) values of this product are represented as yellow (blue). Notice that (i) the striped structure of the order parameter (green and yellow stripes) depicts the idealized underlying variable-thickness topography of the film (crests and valleys, respectively), while (ii) each blue circle appearing in the color plots corresponds to one vortex.

The observed behavior stems from the fact that, initially (and mediated by vortex-vortex interactions), the increasing vortex density stabilizes the lattice with vortices occupying the floor of the undulations. Moreover, as marked in the plot, a nearly hexagonal lattice may be intuited. Such stability hinders vortex mobility across the grooves until eventual hopping occurs in the form of vortex bundles. However, once vortices sufficiently populate the undulations, the vortex lattice no longer drifts collectively, and the vortex dynamics primarily consists of individual vortex hoppings between the grooves. Those hoppings are easier to stimulate by applied current as the vortex density is increased, and then J_c decreases. The transition from a *collective* to *individual* vortex drift regime may be discerned through the simulated vortex dynamics for different values of the applied magnetic field, as shown in the videos provided in the supplementary material (several snapshots appear in Figs. 8B and 8C, where some steps of the evolution are displayed to visualize this behavior). Apparently, the flux flow regimes for the magnetic flux densities $\mu_0 H = 25$ mT and $\mu_0 H = 65$ mT in Fig. 6 fall respectively into the collective and individual hopping regimes.

4. Conclusions

Ultraviolet femtosecond pulsed-laser-irradiation (λ = 343 nm, τ_p = 238 fs) has enabled the formation of surface nanostructures on Nb thin films, which gradually evolve to quasi-1D periodic corrugations

(LIPSS) of lateral periodicity $\Lambda \approx 260$ nm. Our study includes a systematic characterization of a series of polycrystalline Nb thin films in successive stages of the LIPSS formation process, obtained by tuning up the laser pulse energy while keeping other inputs constant.

A direct correlation has been established between the progressive formation of LIPSS and the underlying microstructural changes. The onset of LIPSS formation also triggers: (i) a reduction of the film thickness, pointing towards a certain level of ablation, in agreement with recent work in stainless steel [56]; (ii) a systematic reduction of the lattice parameter a of Nb; and (iii) a small increase of the grain size mainly at the LIPSS' peaks. A moderate variation of the intrinsic superconducting properties accompanies these features. In fact, a well-defined downshift of the $H_{c2}(T)$ line occurs. The similarities between $T_c(E_p)$ and $a(E_p)$ reveal the origin of the variation of T_c induced by the laser treatment [1,5].

Furthermore, the observable lattice compression found for samples fully covered by LIPSS ($\approx 1.05\%$, as compared to the pristine reference) is likely to produce stress in the surrounding areas and this may be the reason for the important decrease of T_c at the boundaries between LIPSS and pristine neighboring areas observed in previous studies [37].

The flux pinning-related properties, specifically the critical current density, are noticeably affected by the laser irradiation process. Changes occur gradually as LIPSS are being formed, anisotropically as concerns the relative orientation of the applied current in experiments, and differently for different operation conditions (applied field and temperature). The increase in critical current density for the optimally treated samples is related to the circulation of currents along the direction of the LIPSS and occurs progressively in parallel to their formation process, as deduced from transport experiments and magneto-optical imaging.

Our findings concerning the induced anisotropic behavior of the laser-irradiated samples have been interpreted in terms of the phenomenological critical state theory, and further supported by mesoscopic scale calculations of the vortex dynamics in undulated samples through the time-dependent Ginzburg–Landau theory. According to both the experimental observations and the simulations, the presence of thickness variations of depth $\lesssim 100$ nm in our films with original thickness of 200 nm produces an effective flux pinning effect that multiplies the critical current density along the channels by a factor of ≈ 2, related to the preference of vortices to settle in the lower thickness region.

In summary, this work delves into the nature of the laser-induced modification of the physical properties of superconducting Nb films. We demonstrate control over the radiation parameters that allow the modification of the physical properties *à la carte*. In fact, we find a correlation between the variation of the fundamental physical parameters (critical temperature, upper critical field, critical current density, and the appearance of anisotropy) with the actual material processing conditions. These results qualify laser-processing as an enabling technology in the fabrication of superconducting circuit elements. Investigation is underway to achieve further control of the surface profiles, including the fabrication of inclined ripple nanostructures, as required in superconducting filters, diodes, and field-resilient ratchets. Although this work focuses on Nb films, the technology may be transferred to other materials, and work is in progress for type-II alloys and high-T_c compounds.

CRediT authorship contribution statement

Javier Frechilla: Writing – review & editing, Writing – original draft, Investigation, Data curation, Conceptualization. **Nicolas Lejeune:** Investigation, Data curation. **Elena Martínez:** Writing – review & editing, Writing – original draft, Formal analysis, Data curation, Conceptualization. **Emile Fourneau:** Visualization, Data curation. **Alejandro Frechilla:** Data curation. **Sergio Martín:** Data curation. **Leonardo R. Cadorim:** Validation, Software, Investigation, Formal analysis. **Luis A. Angurel:** Writing – review & editing, Methodology, Conceptualization, Funding acquisition. **Germán F. de la Fuente:** Conceptualization. **Alejandro V. Silhanek:** Writing – review & editing, Formal analysis, Conceptualization, Funding acquisition. **Milorad V. Milošević:** Writing – review & editing, Supervision, Formal analysis, Conceptualization, Funding acquisition. **Antonio Badía-Majós:** Writing – review & editing, Writing – original draft, Supervision, Funding acquisition, Formal analysis, Data curation, Conceptualization.

Declaration of competing interest

The authors declare that they have no known competing financial interests or personal relationships that could have appeared to influence the work reported in this paper.

Acknowledgments

This publication is part of the projects PID2020-113034RB-I00 (funded by MCIN/AEI/ 10.13039/501100011033), PID2023-146041OB-C21 (funded by MICIU/AEI/10.13039/501100011033 and ERDF/EU), and T54-23R (funded by Gobierno de Aragón, Spain). J.F. acknowledges support from Gobierno de Aragón through predoctoral contracts. N.L. acknowledges the support from FRS-FNRS (Research Fellowships FRIA). The work of E.F. has been financially supported by the FWO and F.R.S.-FNRS under the Excellence of Science (EOS) Project No. O.0028.22. The authors would like to acknowledge the use of Servicio General de Apoyo a la Investigación-SAI (Universidad de Zaragoza) and the Spanish National Facility ELECMI ICTS, node "Laboratorio de Microscopías Avanzadas (LMA)" at "Universidad de Zaragoza". The work of L.R.C. and M.V.M. was sponsored by the Army Research Office, USA and was accomplished under Grant Number W911NF-24-1-0145. The views and conclusions contained in this document are those of the authors and should not be interpreted as representing the official policies, either expressed or implied, of the Army Research Office or the U.S. Government. The U.S. Government is authorized to reproduce and distribute reprints for Government purposes notwithstanding any copyright notation herein. The collaboration in this work has been fostered by the EU-COST Action CA21144 SUPERQUMAP.

Appendix A. TDGL modeling

The simulations were carried out through the numerical solution of the two-dimensional TDGL equation adapted to superconducting films with variable thickness [40].

$$u\left(\frac{\partial}{\partial t}+\mathrm{i}\varphi\right)\psi = \frac{1}{d}(\boldsymbol{\nabla}-\mathrm{i}\mathbf{A})\cdot d\,(\boldsymbol{\nabla}-\mathrm{i}\mathbf{A})\,\psi + \psi(1-|\psi|^2), \tag{A.1}$$

where $d \equiv d(x,y)$ is the thickness profile of the film and u is a constant (≈ 5.79) representing the ratio of relaxation times for the amplitude and phase of the order parameter in dirty superconductors. The order parameter ψ is in units of the field-free order parameter ψ_∞ at the given temperature T; lengths in units of the superconducting coherence length $\xi(T)$; time in units of $t_{GL} = \pi\hbar/8uk_BT_c$; the vector potential $\mathbf{A}$ in units of $H_{c2}\xi$, with H_{c2} being the upper critical field, and the electrostatic potential φ in units of $\hbar/2et_{GL}$. φ is obtained from the Poisson equation:

$$\boldsymbol{\nabla}\cdot(d\boldsymbol{\nabla}\varphi) = \boldsymbol{\nabla}\cdot(d\boldsymbol{J}_s), \tag{A.2}$$

where the supercurrent is given by:

$$\boldsymbol{J}_s = \mathrm{Im}\left[\bar{\psi}(\boldsymbol{\nabla}-\mathrm{i}\mathbf{A})\psi\right]. \tag{A.3}$$

Boundary conditions for ψ are set to guarantee no supercurrent flows out of the film. The applied current is introduced through the boundary condition for φ, with $\boldsymbol{\nabla}\varphi = \boldsymbol{J}_{applied}$ along the surfaces perpendicular to the external current, while $\boldsymbol{\nabla}\varphi = 0$ is set at the remaining surfaces.

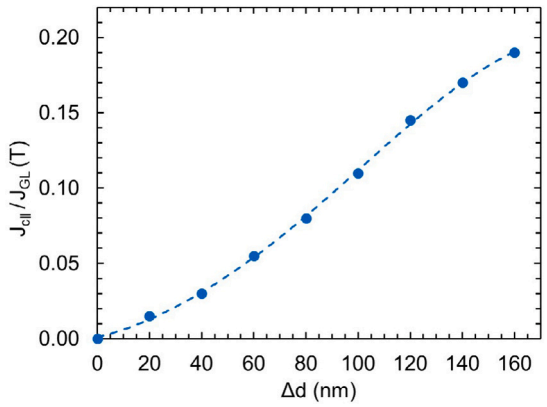

Fig. A.1. TDGL simulations for an infinite (periodic) ideally undulated sample. $J_{c\|}$ obtained from simulations in applied magnetic field $\mu_0 H = 4$ mT, as a function of the depth of thickness undulations, Δd. Dimensionless units are used for J_c in terms of the temperature-dependent Ginzburg–Landau critical current density.

As in experiments, when considered, the external magnetic field will be assumed to be applied along the z-axis, i.e., normal to the film. Details on the numerical discretization can be found in Ref. [57]. Aiming at disclosing the role of surface undulations on the sample's physical properties, simulations were performed by neglecting flux pinning effects other than those linked to thickness variations or edge barriers.

In fact, in order to clearly detach the pure contribution of the undulations to the critical current and "eliminate" the geometrical effect of the edges, we specifically calculated the vortex dynamics in a periodic (infinite) sample, at the same magnetic field and temperature used in Fig. 7 of the main text (Fig. A.1). We recall that in the infinite sample case, one has $J_{c\perp} = 0$, since there is no pinning in the idealized theoretical model to prevent the vortex motion along the thickness grooves. On the other hand, $J_{c\|}$ grows with Δd, as growing undulations increase the effective pinning potential that hampers vortex motion. Remarkably, the $J_{c\|}$ obtained in this case, i.e. $J_{c\|} - 0$ practically corresponds to the difference $J_{c\|} - J_{c\perp}$ seen in the case of a finite sample (Fig. 7C), and thus indeed would represent the contribution of the undulations alone in an ideal sample without additional vortex pinning effects, either coming from background or geometrical pinning. Here, it must be mentioned that real scenarios may be even a bit more complex, because real sample edges are not free from defects that also act as flux penetration points [58]. Nevertheless, again, the reasonable agreement between the simulations for an ideal undulated film and the real AFM topography (Fig. 7D) confirms the prominence of the bulk pinning effect related to the thickness variations.

Appendix B. Supplementary data

Supplementary material related to this article can be found online at https://doi.org/10.1016/j.surfin.2026.109028.

Data availability

The data that support the findings of this article are openly available at [59].

References

[1] S. Bose, P. Raychaudhuri, R. Banerjee, P. Vasa, P. Ayyub, Mechanism of the size dependence of the superconducting transition of nanostructured Nb, Phys. Rev. Lett. 95 (2005) 147003.
[2] A.I. Gubin, K.S. Il'in, S.A. Vitusevich, M. Siegel, N. Klein, Dependence of magnetic penetration depth on the thickness of superconducting Nb thin films, Phys. Rev. B 72 (2005) 064503.
[3] J. Choi, Y.-K. Kim, C.-D. Kim, S. Kim, Y. Jo, Enhancing the critical temperature of strained Niobium films, Mater. Res. Express 7 (7) (2020) 076001.
[4] T. Imamura, T. Shiota, S. Hasuo, Fabrication of high quality Nb/A1O_x–Al/Nb josephson junctions: I– Sputtered Nb films for junction electrodes, IEEE Trans. Appl. Supercond. 2 (1992) 1–14.
[5] J. Liu, J. Li, T. Li, T. Li, W. Wu, W. Chen, Study of stress and morphology of superconducting niobium thin films, IEEE Trans. Appl. Supercond. 19 (2009) 245–248.
[6] H. Gao, S. Wang, D. Xu, X. Wang, Q. Zhong, Y. Zhong, J. Li, W. Cao, Study of DC magnetron sputtered Nb films, Crystals 12 (2022) 31.
[7] Y. Zhong, Z. Ni, J. Li, X. Li, W. Cao, X. Wang, Q. Zhong, J. Xu, C. Liang, Influence mechanism of RF bias on microstructure and superconducting properties of sputtered niobium thin films, Vacuum 207 (2023) 111636.
[8] C.G. Torres-Castanedo, D.P. Goronzy, T. Pham, A. McFadden, N. Materise, P. Masih Das, M. Cheng, D. Lebedev, S.M. Ribet, M.J. Walker, D.A. Garcia-Wetten, C.J. Kopas, J. Marshall, E. Lachman, N. Zhelev, J.A. Sauls, J.Y. Mutus, C.R.H. McRae, V.P. Dravid, M.J. Bedzyk, M.C. Hersam, Formation and microwave losses of hydrides in superconducting niobium thin films resulting from fluoride chemical processing, Adv. Funct. Mater. 24 (2024) 2401365.
[9] S. Karuppannan, D. Huang, N. Kommanaboina, K. Anil, G. Yang, D. Repaka, Y. Zhang, K. Goh, W. Kai, N.L. Chee Beng, Y. Sherry, M. Mukherjee, Improved interface of niobium superconducting resonator with ruthenium as a capping layer, ACS Appl. Electron. Mater. 6 (2023) 7372.
[10] Y. Liu, M. Yang, Y. Fan, Z. Xu, Y. Wu, Y. Liu, W. Peng, G. Mu, Z.-R. Lin, Regulation of superconductivity in Nb thin films induced by interstitial oxygen atoms, Chin. Phys. B 34 (4) (2025) 047401.
[11] S. Savel'ev, F. Nori, Experimentally realizable devices for controlling the motion of magnetic flux quanta in anisotropic superconductors, Nat. Mater. 1 (3) (2002) 179–184,
[12] C.S. Lee, B. Jankó, I. Derényi, A.L. Barabási, Reducing vortex density in superconductors using the 'ratchet effect', Nature 400 (6742) (1999/07/01) 337–340,
[13] J.E. Villegas, S. Savel'ev, F. Nori, E.M. González, J.V. Anguita, R. García, J.L. Vicent, A superconducting reversible rectifier that controls the motion of magnetic flux quanta, Science 302 (5648) (2003) 1188–1191.
[14] A. Silhanek, L. Van Look, S. Raedts, R. Jonckheere, V.V. Moshchalkov, Guided vortex motion in superconductors with a square antidot array, Phys. Rev. B 68 (2003) 214504.
[15] A.V. Silhanek, J. Van de Vondel, V.V. Moshchalkov, Guided vortex motion and vortex ratchets in nanostructured superconductors, in: V. Moshchalkov, R. Wördenweber, W. Lang (Eds.), Nanoscience and Engineering in Superconductivity, Springer Berlin Heidelberg, Berlin, Heidelberg, ISBN: 978-3-642-15137-8, 2010, pp. 1–24.
[16] J. Cuppens, G.W. Ataklti, V.V. Moshchalkov, A.V. Silhanek, J. Van de Vondel, C.C. de Souza Silva, R.M. da Silva, J. Albino Aguiar, Current-induced vortex trapping in asymmetric toothed channels, Phys. Rev. B 84 (2011) 184507.
[17] O.V. Dobrovolskiy, M. Huth, Dual cut-off direct current-tunable microwave low-pass filter on superconducting Nb microstrips with asymmetric nanogrooves, Appl. Phys. Lett. (ISSN: 0003-6951) 106 (14) (2015) 142601.
[18] V.K. Vlasko-Vlasov, F. Colauto, T. Benseman, D. Rosenmann, W.K. Kwok, Triode for magnetic flux quanta, Sci. Rep. 6 (1) (2016/11/15) 36847,
[19] B.Y. Zhu, F. Marchesoni, F. Nori, Controlling the motion of magnetic flux quanta, Phys. Rev. Lett. 92 (2004) 180602.
[20] L. Nulens, N. Lejeune, J. Caeyers, S. Marinković, I. Cools, H. Dausy, S. Basov, B. Raes, M.J. Van Bael, A. Geresdi, A.V. Silhanek, J. Van de Vondel, Catastrophic magnetic flux avalanches in NbTiN superconducting resonators, Commun. Phys. 6 (1) (2023) 267,
[21] A.E. Koshelev, Directional driving of superconducting vortex lines with an oscillating magnetic field, Phys. Rev. Appl. 24 (2025) 034006.
[22] S. Bermon, T. Gheewala, Moat-guarded Josephson SQUIDs, IEEE Trans. Magn. 19 (3) (1983) 1160–1164.
[23] C. Song, M.P. DeFeo, K. Yu, B.L.T. Plourde, Reducing microwave loss in superconducting resonators due to trapped vortices, Appl. Phys. Lett. 95 (23) (2009) 232501.
[24] Y. Pan, G. Wu, D. Zhang, X. Fan, Y. Wang, X. Liu, M. Niu, L. Zhang, J. Ren, Z. Wang, L. Chen, Magnetic imaging of abrikosov vortices trapped near moats in the niobium thin film, Supercond. Sci. Technol. 38 (2) (2025) 025011.
[25] C. Reichhardt, C.J.O. Reichhardt, M.V. Milošević, Statics and dynamics of skyrmions interacting with disorder and nanostructures, Rev. Modern Phys. 94 (2022) 035005.
[26] N. Del-Valle, S. Agramunt-Puig, A. Sánchez, C. Navau, Imprinting skyrmions in thin films by ferromagnetic and superconducting templates, Appl. Phys. Lett. 107 (13) (2015) 133103.
[27] R.M. Menezes, J.F.S. Neto, C.C. de Souza Silva, M.V. Milošević, Manipulation of magnetic skyrmions by superconducting vortices in ferromagnet-superconductor heterostructures, Phys. Rev. B 100 (2019) 014431.

[28] J. Bonse, J. Krüger, Structuring of thin films by ultrashort laser pulses, Appl. Phys. A 129 (2023) 14.
[29] X. Chen, T. Huang, R. Li, Y. Lin, J. Yang, W. Li, W. Yu, Femtosecond laser-processed perovskite thin films with reduced nonradiative recombination and improved photodetecting performance, ACS Appl. Electron. Mater 5 (2023) 3316–3323.
[30] A. Sharif, N. Farid, M. Wang, K. Choy, G. O'Connor, The role of fluence in determining the response of thin molybdenum films to ultrashort laser irradiation; from laser-induced crystallization to ablation via photomechanical ablation and nanostructure formation, Appl. Surf. Sci. 592 (2022) 153315.
[31] V. Lapidas, A. Cherepakhin, A. Kozlov, A. Shevlyagin, K. Kolonica, S. Shevlyagina, A. Kokhanovskiy, J. Zhang, A. Zhizhchenko, A. Kuchmizhak, Structural coloration on titanium films by direct femtosecond laser patterning empowered by neural networks, ACS Appl. Mater. Interfaces 17 (2025) 16122–16131.
[32] E. Skoulas, A. Tasolamprou, G. Kenanakis, E. Stratakis, Laser induced periodic surface structures as polarizing optical elements, Appl. Surf. Sci. 541 (2021) 148470.
[33] K. Vilkevičius, A. Tsibidis, E. Stratakis, E. Stankevičius, Formation of highly tunable periodic plasmonic structures on gold films using direct laser writing, Adv. Opt. Mater. 12 (2024) 2400172.
[34] A. Cubero, E. Martínez, L. Angurel, G. de la Fuente, R. Navarro, H. Legall, J. Krüger, J. Bonse, Effects of laser-induced periodic surface structures on the superconducting properties of Niobium, Appl. Surf. Sci. 508 (2020) 145140.
[35] A. Cubero, E. Martínez, L.A. Angurel, G.F. de la Fuente, R. Navarro, H. Legall, J. Krüger, J. Bonse, Surface superconductivity changes of niobium sheets by femtosecond laser-induced periodic nanostructures, Nanomaterials 10 (12) (2020) 2525.
[36] A. Badía-Majós, E. Martínez, L.A. Angurel, G. de la Fuente, E. Fourneau, S. Marinković, A. Silhanek, Laser nanostructured metasurfaces in Nb superconducting thin films, Appl. Surf. Sci. (ISSN: 0169-4332) 649 (2024) 159164.
[37] E. Martínez, N. Lejeune, J. Frechilla, L. Porta-Velilla, E. Fourneau, L.A. Angurel, G.F. de la Fuente, J. Bonse, A.V. Silhanek, A. Badía-Majós, Laser engineered architectures for magnetic flux manipulation on superconducting Nb thin films, Appl. Surf. Sci. 679 (2025) 161214.
[38] JCPDS-International Centre for Diffraction Data, 2000.
[39] G. Shaw, J. Brisbois, L.B.G.L. Pinheiro, J. Müller, S. Blanco Alvarez, T. Devillers, N.M. Dempsey, J.E. Scheerder, J. Van de Vondel, S. Melinte, P. Vanderbemden, M. Motta, W.A. Ortiz, K. Hasselbach, R.B.G. Kramer, A. Silhanek, Quantitative magneto-optical investigation of superconductor/ferromagnet hybrid structures, Rev. Sci. Instrum. (ISSN: 0034-6748) 89 (2018) 023705.
[40] S. Chapman, Q. Du, M. Gunzburger, A model for variable thickness superconducting thin films, Z. Angew. Math. Phys. ZAMP 47 (3) (1996) 410–431.
[41] K. Bronnikov, A. Dostovalov, V. Terentyev, S. Babin, A. Kozlov, E. Pustovalov, E.L. Gurevich, A. Zhizhchenko, A. Kuchmizhak, Uniform subwavelength high-aspect ratio nanogratings on metal-protected bulk silicon produced by laser-induced periodic surface structuring, Appl. Phys. Lett. (ISSN: 0003-6951) 119 (21) (2021) 211106.
[42] F. Fraggelakis, P. Lingos, G.D. Tsibidis, E. Cusworth, N. Kay, L. Fumagalli, V.G. Kravets, A.N. Grigorenko, A.V. Kabashin, E. Stratakis, Double-pulse femtosecond laser fabrication of highly ordered periodic structures on au thin films enabling low-cost plasmonic applications, ACS Nano 19 (25) (2025) 23258–23275.
[43] D.K. Finnemore, T.F. Stromberg, C.A. Swenson, Superconducting properties of high-purity niobium, Phys. Rev. 149 (1966) 231–243.
[44] E.H. Brandt, Square and rectangular thin superconductors in a transverse magnetic field, Phys. Rev. Lett. 74 (1995) 3025–3028.
[45] F. Colauto, M. Motta, W.A. Ortiz, Controlling magnetic flux penetration in low-Tc superconducting films and hybrids, Supercond. Sci. Technol. 34 (1) (2020) 013002.
[46] D.-X. Chen, A. Sanchez, J. Nogues, J.S. Muñoz, Bean's, Kim's, and exponential critical-state models for high-T_c superconductors, Phys. Rev. B 41 (1990) 9510–9512.
[47] E.H. Brandt, Electric field in superconductors with rectangular cross section, Phys. Rev. B 52 (1995) 15442–15457.
[48] A. Sánchez, C. Navau, Critical-current density from magnetization loops of finite high-T_c superconductors, Supercond. Sci. Technol. 14 (7) (2001) 444.
[49] E.M. Gyorgy, R.B. van Dover, K.A. Jackson, L.F. Schneemeyer, J.V. Waszczak, Anisotropic critical currents in $Ba_2YCu_3O_7$ analyzed using an extended bean model, Appl. Phys. Lett. (ISSN: 0003-6951) 55 (3) (1989) 283–285.
[50] P. Martinoli, O. Daldini, C. Leemann, E. Stocker, A.c. Quantum interference in superconducting films with periodically modulated thickness, Solid State Commun. (ISSN: 0038-1098) 17 (2) (1975) 205–209.
[51] T. Schuster, M.V. Indenbom, M.R. Koblischka, H. Kuhn, H. Kronmüller, Observation of current-discontinuity lines in type-II superconductors, Phys. Rev. B 49 (1994) 3443–3452.
[52] C. Jooss, J. Albrecht, H. Kuhn, S. Leonhardt, H. Kronmüller, Magneto-optical studies of current distributions in high-Tc superconductors, Rep. Progr. Phys. 65 (5) (2002) 651.
[53] A.K. Niessen, J. Van Suchtelen, F.A. Staas, W.F. Druyvesteyn, Guided motion of vortices and anisotropic resistivity in Type-II superconductors, Philips Res. Rep. 20 (1965) 226–234.
[54] D.D. Morrison, R.M. Rose, Controlled pinning in superconducting foils by surface microgrooves, Phys. Rev. Lett. 25 (1970) 356–359.
[55] O. Daldini, P. Martinoli, J.L. Olsen, G. Berner, Vortex-line pinning by thickness modulation of superconducting films, Phys. Rev. Lett. 32 (1974) 218–221.
[56] R. Wonneberger, S. Gräf, J. Bonse, W. Wisniewski, K. Freiberg, M. Hafermann, C.R.F.A. Müller, A. Undisz, Tracing the formation of femtosecond Laser-Induced Periodic Surface Structures (LIPSS) by implanted markers, ACS Appl. Mater. Interfaces 17 (2025) 2462–2468.
[57] M.V. Milošević, R. Geurts, The Ginzburg–Landau theory in application, Phys. C: Supercond. 470 (19) (2010) 791–795.
[58] A.V. Silhanek, L. Jiang, C. Xue, B. Vanderheyden, Impact of border defects on the magnetic flux penetration in superconducting films, Appl. Phys. Rev. 12 (4) (2025) 041324.
[59] J. Frechilla, N. Lejeune, E. Martínez, E. Fourneau, A. Frechilla, S. Martín, L.R. Cadorim, L.A. Angurel, G.F. de la Fuente, V.A. Silhanek, M.V. Milošević, A. Badía-Majós, Zenodo, 2025. http://dx.doi.org/10.5281/zenodo.15761919.